Materials Characterization 164 (2020) 110327

Contents lists available at ScienceDirect

Materials Characterization

journal homepage: www.elsevier.com/locate/matchar

Element segregation and α_2 formation in primary α of a near-α Ti-alloy

Claudius Dichtl[a,*], Zhenbo Zhang[a], Hazel Gardner[b], Paul Bagot[b], Anna Radecka[e], David Dye[c], Matthew Thomas[d,f], Rebecca Sandala[e], João Quinta da Fonseca[a], Michael Preuss[a]

[a] University of Manchester, Manchester, M13 9PL, UK
[b] University of Oxford, Oxford, OX1 3PH, UK
[c] Imperial College London, London SW7 2AZ, UK
[d] TIMET, PO Box 704, Witton, B6 7UR, UK
[e] Rolls-Royce plc, Derby, DE24 8BJ, UK
[f] The Manufacturing Technology Centre, Ansty Park, Coventry CV7 9JU, UK

ARTICLE INFO

Keywords:
Titanium alloys
Chemical partitioning
Electron probe micro analysis (EPMA)
Transmission electron microscopy (TEM)
Atom probe tomography (APT)

ABSTRACT

Alloy TIMETAL®834 is a near-α Ti-alloy typically processed to have a complex bimodal microstructure that provides a good combination of mechanical properties at temperatures in excess of 450 °C. Due to the high Al content, typical ageing procedures result in the formation of intragranular and coherent nano-scale Ti_3Al precipitation (α_2), which increase strength but also promotes slip planarity. The present study focuses on chemical partitioning as a result of sub-β-transus heat treatment and the consequences for the two different constituents in the bimodal microstructure. The detailed chemical and structural analysis were carried out by combining Electron **P**robe **M**icro **A**nalysis (**EPMA**), **W**avelength **D**ispersive **Sp**ectroscopy (**WDS**), **T**ransmission **E**lectron **M**icroscopy (**TEM**) and **A**tom **P**robe **T**omography (**APT**) for investigating local compositional variations and their effect on the formation of α_2 precipitates. Detailed microchemical analysis shows a core-shell composition arrangement of α-stabilisers with the shell composition similar to the one of secondary α. Selected area electron diffraction in the TEM and APT analysis demonstrates that those local variations in α stabilisers affect the level of α_2 precipitation. In addition, EPMA maps show that while Zr and Sn are often considered to be neutral alloying elements in Ti-alloys, they do segregate to the β-phase during sub-β-transus heat treatment.

1. Introduction

In typical two-phase Ti-alloys, the α phase is strengthened by solution-strengthening and in some cases also precipitation strengthening. Solution strengthening is achieved by the addition of α-stabilising and neutral elements such as Al, O, Sn and Zr. These elements display fairly large differences in atomic radii compared to Ti, but at the same time show sufficiently high solid solubility limits in the α-titanium matrix [1]. The difference in size results in lattice strain, which affects the mobility of dislocations and therefore causes a strengthening effect [2,3]. According to Collings et al., the strengthening effect of alloying elements is based on the electron states of the alloying elements, i.e. the formation of tight and directional bonds between the alloying and titanium atoms [4]. In the range of 0–15 at.%, the strengthening effect of aluminium in solid solution is linearly proportional to the concentration of aluminium [3]. However, it is well established that commercial two-phase titanium alloys that contain at least 5 wt% aluminium can form Ti_3Al (α_2) precipitates when aged below the α_2 solvus [5]. According to Namboodhiri et al., an aluminium concentration of over 13 at.% is required for obtaining α_2 precipitation when the material is aged at 700 °C [6]. However, this value applies for the overall composition of the alloy and doesn't consider local variations in the aluminium concentration. In addition, some work has demonstrated that short-range ordering might take place before α_2 precipitation is observed [6]. A detailed analysis by Atom Probe Tomography (APT) on the evolution of α_2 precipitates with ageing time and temperature has been carried out by Radecka et al. [7,8]. This work has shown that zirconium, silicon, molybdenum and vanadium accelerate the formation of α_2 precipitates, compared to pure Ti-Al systems. It was also found that tin and silicon are stronger α_2 formers than aluminium and therefore can replace aluminium atoms in α_2.

The situation regarding α_2 formation is further complicated in titanium alloys with bimodal microstructures since during solution treatment below the β-solvus, aluminium partitions to the primary α phase. Upon cooling, sufficiently fast to trigger the formation of secondary α rather than exclusive growth of primary α, the concentration

* Corresponding author.
E-mail address: Claudius.dichtl@manchester.ac.uk (C. Dichtl).

https://doi.org/10.1016/j.matchar.2020.110327
Received 13 January 2020; Received in revised form 2 April 2020; Accepted 16 April 2020
Available online 19 April 2020

of α-stabilising elements is lower in the secondary α than in the primary α constituent. Since aluminium is the main α-stabilising element and also has the most significant effect on solid-solution strengthening, primary α might be the stronger of the two α constituents. However, secondary α tends to have a very fine lath structure providing Hall-Petch strengthening. An interesting aspect of the bimodal microstructure evolution is that unless the material is quenched at very fast rates, primary α grains can also grow by up to a few microns [9].

TIMETAL®834 (Ti-5.8Al-4Sn-3.5Zr-0.7Nb-0.5Mo-0.35Si-0.06C) is a near-α titanium alloy, which is typically processed to display a bimodal microstructure and a primary α volume fraction of approximately 10 to 15% [10]. This alloy has been developed for applications in jet-engines with temperature capabilities well in excess of 450 °C through the minimisation of β phase, utilisation of molybdenum and niobium instead of vanadium as a β-stabiliser, addition of 4 wt% Sn and about 0.3 wt% Si to enhance creep performance. The relatively high levels of aluminium and tin TIMETAL®834 are known to lead to a significant level of α_2 precipitation in the α phase [11–13].

In the present work, detailed microstructural and chemical analyses have been carried out to shed new light on the segregation of alloying elements in a bimodal microstructure of TIMETAL®834 caused by α + β solution treatment, and on the consequences these have on α_2 formation using a variety of electron microscopy techniques and APT analysis.

2. Experimental

2.1. Sample preparation

Forged TIMETAL®834 ingot material was supplied by TIMET, UK. The as-received material was solution heat-treated below the β-solvus at 1015 °C for 2 h followed by cooling the material to ambient temperature at a cooling rate of 1 K/s resulting in a bimodal microstructure with a lamella-spacing of around 2.5 μm. Material was subsequently aged for 2 h at 700 °C which is known to promote α_2 precipitation [7].

For imaging of the microstructure in the SEM and microchemical analysis, samples were prepared using standard metallographic procedures: grinding with abrasive SiC-paper of 4000 grit and polishing in colloidal-silica suspension. Foils for transmission electron microscopy were prepared by grinding (800 grit SiC-paper) material to a thickness of around 100 μm before punching out 3 mm diameter discs and electropolish those in a TENUPOL5 (Struers) twin-jet polisher using 10% perchloric acid, 90% methanol solution at a temperature of −32 °C in order to achieve a region that is electron-transparent.

Samples for APT were prepared using focused-ion-beam (FIB) milling. Etched samples were used to enhance the contrast in secondary electron (SE) imaging. First, a cantilever-beam was machined from a single grain, along the same cross-section for which the concentration profile had been measured by EPMA (see Fig. 3). APT-needles with a tip radius of < 100 nm [14,15] were prepared from this beam at equal distances, giving samples at different distances from the grain/interface boundary.

2.2. Scanning electron microscopy and electron backscatter diffraction (EBSD)

Back-Scattered-Electron (BSE)-SEM imaging at 15 keV was used for the morphological analysis of the microstructure. BSE contrast can be sensitive to crystallographic orientation and chemical variations. If the contrast in an image arises from the chemical composition, higher brightness correlates to areas with higher densities and higher atomic numbers than in the darker regions [16]. In order to distinguish between chemical and orientation contrast, grain orientation mapping was carried out in addition to BSE-SEM imaging using Electron-Back-Scattered-Diffraction (EBSD) in an SEM at an acceleration voltage of 15 keV and a step size of 0.2 μm. For both imaging modes, an FEI Quanta 650 Field Emission Gun Scanning Electron Microscope (FEG-SEM) was utilised equipped with an Oxford Instruments HKLNordlys EBSD detector.

2.3. Electron-probe microanalysis EPMA-WDS

Microchemical analysis was carried out using a Jeol JXA-8230 electron-probe-microanalysis (EPMA) with Wavelength-Dispersive-Spectroscopy (WDS). In this method, an electron beam is scanned over the sample and the intensities of the emitted X-rays are measured as a function of the wavelength of the photons. The chemical composition is determined based on the characteristic X-rays emitted by the analysed material [17].

The microchemical analysis was carried out at an acceleration voltage of 7 keV, as a Monte-Carlo-simulation using Casino v2.48′ [18] showed that at this voltage the interaction volume is < 300 nm in width and depth for TIMETAL®834. Therefore, the interaction volumes of two adjacent scanning points are not overlapping for mapping or line-scans at a step size of 1 μm. Two types of datasets were recorded for the microchemical analysis: qualitative maps to assess spatial distribution for each analysed element and quantitative line-scans. For the latter, the EPMA was calibrated using standards for each element prior to the line-scan. Line-scans were taken along the cross-sections of primary α grains to quantify the difference in chemical composition caused by element partitioning. The average relative error of the chemical composition for Al was 1.1%, correlating to an absolute error of 0.06 wt%. As error bars would be of a similar size as the symbols used, they are not included in the figures. For all other elements, the absolute error was smaller than the one for Al.

In areas of higher density or where the concentration of elements with larger atomic number is higher, more X-ray Bremsstrahlung is generated, resulting in higher continuous background. When background signal is not compensated in the data processing, higher continuous background could result in an overestimation of the concentration of other elements. Background signal was compensated for in the quantitative line-scans, but not for the qualitative maps.

2.4. Transmission electron microscopy (TEM)

TEM characterisation was performed on a FEI Tecnai TF20 microscope operating at 200 kV. Selected Area Electron Diffraction (SAED) was used to quantify the intensity of the superlattice reflections from the ordered α_2 precipitates in order to obtain qualitative information about α_2 volume fraction changes [19]. In order to achieve this, primary α grains were investigated along the [11–20] zone axis. Diffraction patterns were recorded for several positions along the cross-section of a primary α grain, similar to the line scan taken in the EPMA-WDS analysis. As the intensity of the superlattice reflection spots tends to be very weak compared to the fundamental reflections, DITABIS imaging plates were used for recording the diffraction patterns, providing an exceptional high dynamic range. After recording the diffraction patterns, the plates were removed from the TEM and scanned in an image-plate-scanner (DITABIS Micron) to retrieve the digital images [20].

The intensity of the α_2 superlattice reflections is affected by the accurate alignment of the grain along the given zone-axis and the thickness of the foil. For this reason, the integrated intensities of the superlattice reflections were normalised by the integrated intensities of the corresponding fundamental reflections sitting between the superlattice reflections. The diffraction spots were fitted utilising a Voigt-function [21]. Effects of the background were compensated by subtracting a line from the intensity profile that goes through the minima on both sides of the peak.

2.5. APT

The experiment was carried out using a CAMECA Local Electrode

Atom Probe (LEAP) 5000XR (at a stage temperature of 50 K and with a 50 pJ laser pulse energy) and post-processing and data analysis utilised the CAMECA IVAS software. [22]

Pearson coefficient (μ) values [23] were calculated for each of the three atom probe samples. The two atom probe samples nearest the centre of the alpha grain had a higher μ value (0.09 and 0.08) than the sample nearest the grain boundary (0.04), indicating a higher degree of non-randomness in the centre-grain samples. All three μ values were much greater than the μ value measured for a random solid solution, demonstrating statistical significance.

Aluminium isoconcentration surfaces were used to identify the precipitates in the atom probe datasets. Proximity histograms (proxigrams) were generated for a range of isoconcentration values. Proxigram interface width, calculated using the method described by Homma et al. [24], was plotted as a function of isoconcentration value. An isoconcentration value of 12 at.% Al was selected, as this corresponded to a narrow interface thickness for both the centre-grain samples. Ions contained within this isoconcentration surface were identified as belonging to the α_2 precipitates, and were extracted. Only isoconcentration surfaces that did not intersect the edge of the atom probe dataset were considered.

During an atom probe experiment, evaporation artefacts can cause density fluctuations. To distinguish between these artefacts and chemical clustering, the mass-to-charge values of the datapoints in each of the atom probe datasets were randomly exchanged. 12 at.% Al isoconcentration values were created on these 'randomised' datasets, and any precipitates extracted were considered to be 'random' precipitates resulting from the evaporation artefacts. To control the number of 'random' precipitates included in the analysis, a precipitate cut off volume was chosen such that the percentage of clusters identified in the randomised dataset is < 5% of those observed in the as-measured, experimental dataset. i.e. $(N_{real}\text{-}N_{rand})/N_{real} \geq 95\%$, where N_{real} is defined as the number of precipitates identified in the as-measured, experimental dataset and N_{rand} is defined as the number of precipitates identified in the randomised dataset. The procedure is similar to that outlined in the paper by Williams et al. [25].

Once extracted, the composition of the precipitates was measured, taking into account mass spectrum peak overlaps as described by London [26]. Precipitate volume fraction was calculated by taking the number of ions within the precipitates and dividing by the number of ions within the whole dataset.

The small size of the precipitates in the present case (~2 nm radius) means that the spatial resolution of atom probe is being pushed to the detectable limit. In a study on the effective spatial resolution limits of APT, De Geuser et al. reported that it is possible to detect particles with radius of approximately 1 nm, but that in this case the accuracy of the determined particle size and composition is limited [27]. This means that qualitative comparisons between datasets are appropriate, but quantitative conclusions from absolute numbers of cluster sizes and volume fractions should be treated with some caution.

3. Results

3.1. Observation of a core and shell structure in primary α grains

Water quenching thinner sections of TIMETAL®834 has shown that α + β solution heat treatment at 1015 °C results in a primary α volume fraction of 15 to 16%. However, due to primary α grain growth, the primary α volume fraction, when cooled at 1 K/s, was determined to be 25%. The average grain size of primary α grains is 21 ± 9 μm, with some of the grains exhibiting an elongated shape. A core-shell structure was observed in primary α grains, both in optical (not shown here) and BSE-SEM images. Fig. 1a and Fig. 2a and c are examples of such core-shell structures with darker inner areas and brighter areas close to the grain boundaries. The shell width is 2–6 μm and the volume fraction of the inner darker area was determined to be close to the expected value of 15%. Fig. 2 also shows an example of primary α grains being clustered together. Here, three grains are connected to each other, with each of them exhibiting core-shell structures apart from the region where they contact each other.

3.2. Analysis of crystallographic orientation and crystal structure

In order to explore the possibility of a crystallographic orientation effect causing the core-shell appearance, primary α grains were further analysed by EBSD-based orientation mapping. However, as can be seen in Fig. 1b, the Euler map clearly shows misorientation-free primary α grains with no indication of any substructure within the grains. Further, Fig. 1c also confirms only very small misorientations within 0.3° along trace 1 indicated in Fig. 1b. In the case of the primary α grain below (orange grain in Fig. 1b), an additional distinct contrast can be observed next to the core-shell structure in Fig. 1a. The line scan along trace 2 confirms a misorientation step at around 6–8 μm, at which the crystallographic orientation changes by over 1°, corresponding well with the dark appearance in that particular grain. On both sides of the step, the misorientation variation again stays below 0.3°. Hence, the observed shell structure in the BSE-SEM images is not related to any orientation changes within the primary α grains.

3.3. Analysis of the chemical gradient using EPMA-WDS

In order to relate the core-shell appearance to possible chemical variations within the primary α grains, qualitative chemical maps were recorded in the same regions by EPMA-WDS. Fig. 2b and d show detailed aluminium maps, highlighting that aluminium concentration is generally higher in primary α grains compared to the transformed β-phase region, including secondary α. As expected, the aluminium content is lowest within the β phase. The aluminium map reveals clearly a core-shell structure within primary α that aligns well with the one observed in BSE-SEM images. The centre of the primary α grains is enriched in aluminium, while the outer area is depleted. The chemical distribution is homogeneous within these areas on this length-scale. It is also noticeable that the concentration of aluminium in the outer areas of the primary α grains is similar to the concentration in the secondary α phase, presumably because they are both formed at similar temperatures, during cooling at the end of the solution heat treatment. In the centre of the map, three grains are clustered together. These grains are shown at higher magnification in Fig. 2c & d. At the points where the grains are in contact with each other, the shell is interrupted, and the cores are in direct contact. Therefore, there is a line between two adjacent grains, where no chemical gradient can be observed. Towards the triple point in the centre of these three grains, the depleted shell is narrower with a thickness of 1 to 2 μm. In the BSE-SEM images, additional areas of varying contrast can be observed within primary α grains. This structure does not show up in the chemical distribution map of aluminium and is most likely related to slight orientation variations as already highlighted for the orange grain in Fig. 1.

In Fig. 3 qualitative chemical distribution maps are shown for the β-stabilising elements molybdenum, niobium and silicon (a - c) and the neutral alloying elements tin and zirconium (d & e). The chemical distribution of Mo and Nb is exactly opposite to the one of Al; the concentrations are high in the β-phase, lower in the secondary α phase and lowest in primary α phase. The chemical map of Mo (Fig. 3a) also shows a core-shell structure within primary α grains, with the concentration being lower in the core and higher in the shell. Hardly any Mo signal was recorded from the centre of the primary α grains. The niobium, silicon and zirconium maps also indicate a core-shell structure, with slightly increased concentrations in the shell, but in this case, the contrast is significantly weaker than for Al and Mo. Considering that Zr is usually seen as a neutral element, this observation seems surprising. Sn, also usually considered a neutral alloying element, clearly shows higher concentrations in the transformed β phase region

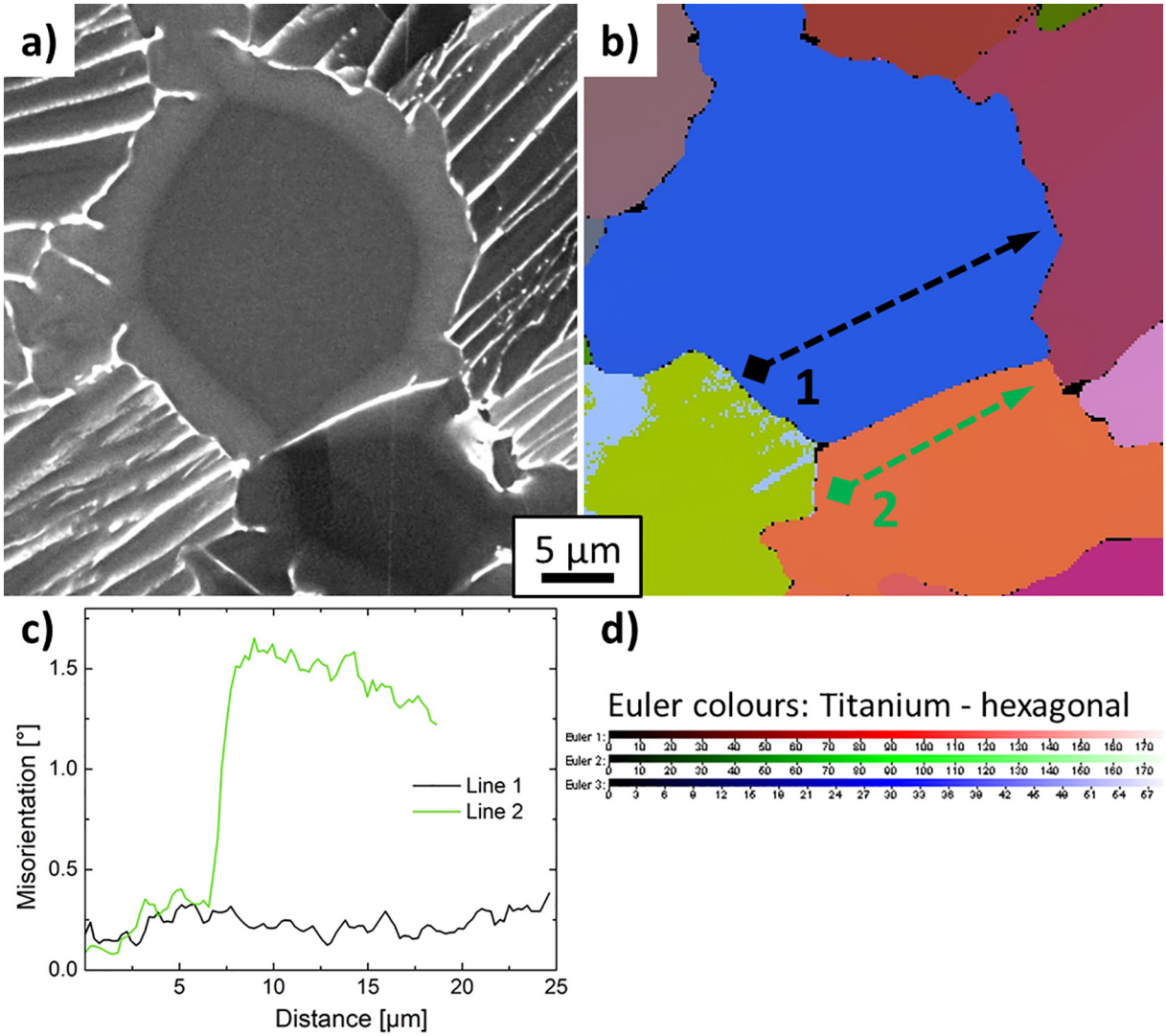

Fig. 1. a) BSE-SEM image of two primary α grains, **b)** crystallographic orientation map (α phase) of the same area, using Euler-colours **d)**. The misorientation along the black (1) and green (2) lines, in reference to the starting point (square), are displayed in figure **c).** (For interpretation of the references to colour in this figure legend, the reader is referred to the web version of this article.)

compared to primary α. In addition, there are indications that Sn reaches higher levels at β triple points.

Fig. 4 shows a BSE-SEM image of a primary α grain together with quantitative concentrations of 6 elements (Al, Sn, Zr, Si, Nb and Mo) taken from an EPMA-WDS line scan recorded across that particular primary α grain. The concentration was measured at equidistant points with spacing of 1 µm. The locations of the primary α grain boundaries related to the EPMA-WDS line scan are indicated by two dashed lines in Fig. 4a and b. The concentration profile confirms the observations from the qualitative chemical maps: the core of the primary α grains is enriched in Al and depleted in all other alloying elements. Towards the grain boundary, the concentrations of Mo, Nb, Sn and Zr increase significantly. For these elements, this effect is very pronounced, e.g. for Mo, the concentration is up to approximately 30 times higher than in the centre of the grain. For Si, this effect is less pronounced and the EPMA analysis indicates a concentration in the β-phase, which is only 50% higher, compared to the primary α phase. It is also noticeable that the element concentrations change several microns before the primary α grain boundaries showing significant chemical variations within the shell structure of the primary α grain. For example, the concentration of aluminium drops from 6 mass.% to 4.5 mass.% about 1 µm before the grain boundary. The same effect applies for all other elements, but instead of decreasing, the concentrations increase when getting closer towards to grain/interface boundary.

3.4. TEM and SAED analysis

Fig. 5 shows a primary α grain highlighting the selected areas where diffraction patterns were recorded. Accordingly, Fig. 6 shows selected area diffraction patterns taken along the [11–20] zone axis from near the grain boundary (a) and the centre of the grain (b). For the diffraction patterns recorded near the grain boundaries, only diffraction spots of the matrix can be observed, while further inside the grain the typical α_2 superlattice reflections are observed. These differences were further confirmed by plotting the line intensity profile through the (0000) diffraction spot, Fig. 6c and d. Hence, the initial observation implies that α_2 precipitates are present in the centre of the grain and that there is less or no α_2-precipitation closer to the grain boundaries.

To analyse the variations in α_2 precipitation as a function of distance from the grain boundary, the ratio of integrated intensities of the superlattice to matrix diffraction spots is plotted in Fig. 7. It can be seen that four points in the centre of the grain (Fig. 5) have similar values, forming a plateau region, indicating the strong presence of α_2 in this region at least 5 µm away from the grain boundary. For both of the

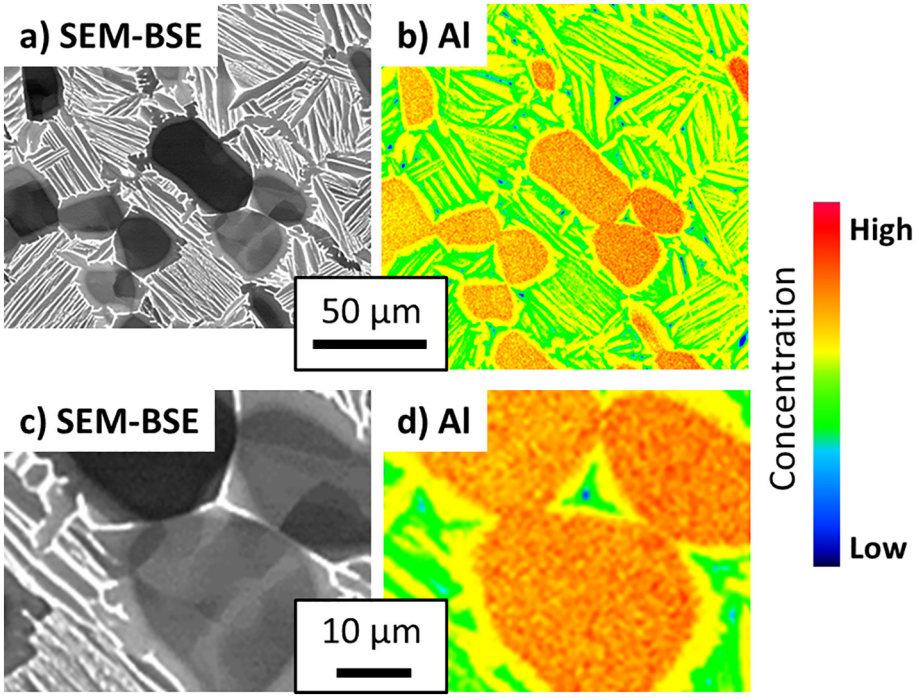

Fig. 2. Electron-Probe-Micro-Analysis (EPMA) of several primary α grains, showing the SEM-BSE-image (**a** & **d**) and qualitative chemical map recorded using wavelength-dispersive-spectroscopy (WDS) of aluminium (**b** & **d**). In image (**c** & **d**) a region of the maps (**a** & **b**) is displayed at a higher magnification.

areas that are closest to the grain boundary (< 2 µm away from the grain-boundary), no superlattice diffraction spots are observed and consequently the intensity ratio is zero. In the transition regions from the grain boundaries towards the centre of the grain (points 2 and 7), superlattice diffraction spots can be observed, but their intensity is lower than in the centre of the grain. This applies for both sides of the grain, but on the right side of the grain, the change in intensity appears steeper than on the left side. It can be seen in Fig. 5 that on the right, the line on which the analysed areas are aligned is perpendicular to the grain boundary, while there is a bulge on the left side of the grain. Therefore point 2 might be closer to grain boundaries than point 7 (see Fig. 4). It needs to be kept in mind that a 2D-cross section has been analysed, not considering the 3D-shape of the grain. 3D-geometry effects could lead to variations of the chemical gradient near the grain boundary, e.g. as it has been observed in Fig. 4 and influence α_2 precipitation.

3.5. APT analysis

Average concentrations have been calculated for three APT-specimens and these are summarised in Table 1. The results have been plotted together with the concentration profile of the EPMA-WDS analysis in Fig. 4. For the two samples in the centre of the grain, the results of both techniques align well. Only for the Sn concentration, the values determined by APT are significantly lower than the ones from EPMA-WDS. One possible explanation is that Sn has a lower evaporation field than Ti and the other alloying elements [28], which means all Sn ions may not be evaporating on the laser pulses as intended. When

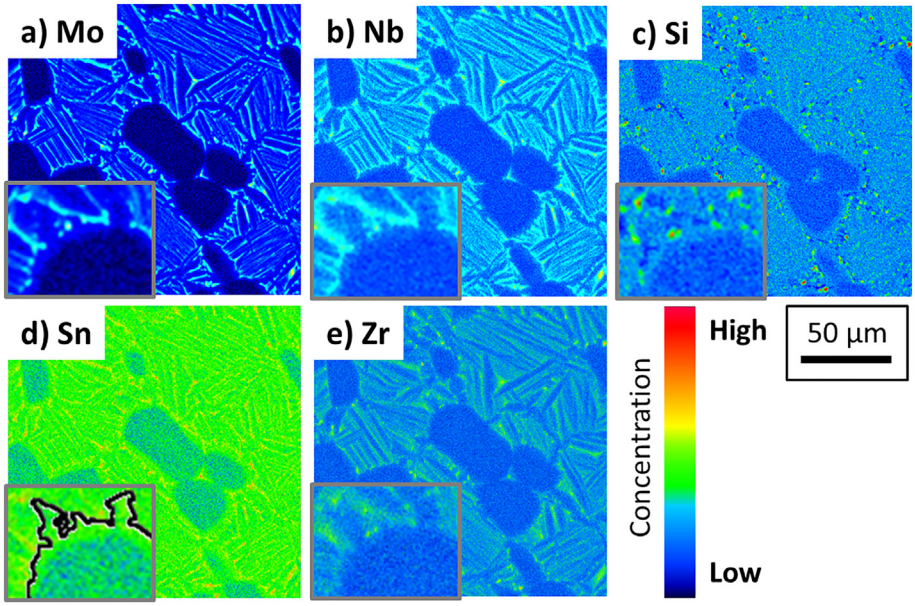

Fig. 3. Qualitative chemical maps recorded using EPMA-WDS for the same area shown in Fig. 3. for the β-stabilising elements molybdenum, niobium and silicon (**a - c**) and the neutral alloying elements tin and zirconium (**d** & **e**). Insets (width 30 µm) display the boundary between primary α grains and transformed β at a higher magnification. Grains boundaries are highlighted by a black line for the map of tin (**d**).

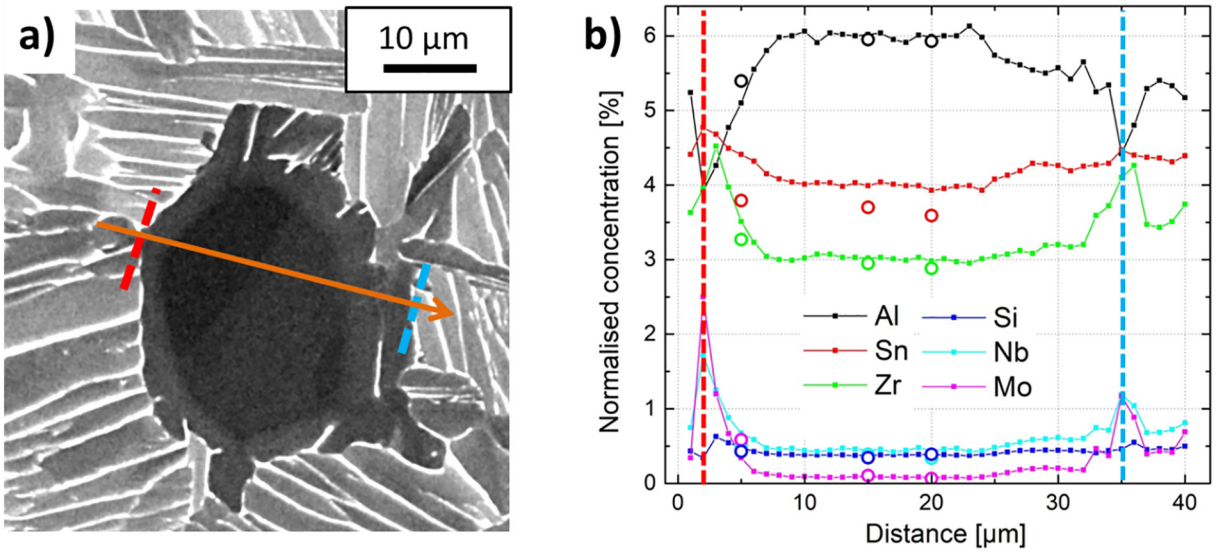

Fig. 4. a) BSE-SEM image of a primary α grain analysed by EPMA, the orange line shows the location of the line scan for the quantitative WDS-analysis. The crystallographic orientation map of the grain is attached in the appendix. It shows that the grain has only one crystallographic orientation. **b)** The normalised concentration along the black line is displayed for Al, Sn, Zr, Si, Nb and Mo. The grain boundaries of the primary α grain are marked with a red and a blue dashed line. Open circles show the average concentrations that have been calculated for the three APT-data sets. (For interpretation of the references to colour in this figure legend, the reader is referred to the web version of this article.)

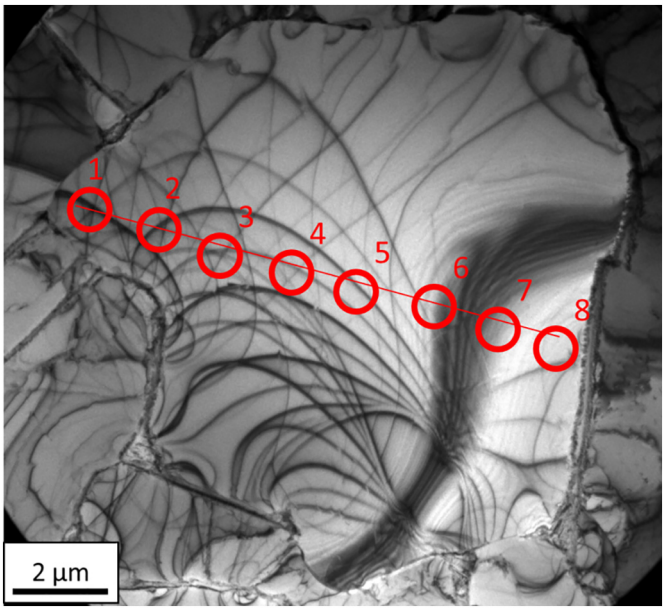

Fig. 5. TEM images of primary α: the red circles (1–8) indicated position within grains where diffraction patterns have been recorded using selective area aperture. (For interpretation of the references to colour in this figure legend, the reader is referred to the web version of this article.)

moving closer to the grain boundaries, both techniques are showing the same trend: the concentration of Al decreases, while the concentration increases for all other elements.

The atom maps for the three needles, seen in Fig. 8, show precipitates in the two needles nearest the centre of the grain (needle 1&2), but not in the needle near the grain boundary (needle 3). When a 12 at. % Al isoconcentration surface was applied to needle three, in line with the standardised analysis method described in Section 2.5, no precipitates were seen; it was not possible to identify any precipitates lower than 12 at.% Al using this analysis method. Thus, while it cannot be said that there is no precipitation in needle 3, there is a greater degree of precipitation in needles 1 and 2 than in needle 3.

The compositions of the precipitates in needles 1 and 2 are reported in Table 2 as 15.7–16.1 at. % Al and 79.1–79.5 at. % Ti. The precipitates are rich in aluminium and the concentration is close to that reported for the α_2 phase; 75 at.% Ti and 22.5–39 at.% Al [29]. α_2 precipitates also contain Sn and Si with an expected Ti:(Al,Sn,Si) ratio of 3:1 [7]. For the analysed particles the concentration of α_2 stabilising elements is lower than expected, with a Ti:(Al,Sn,Si) ratio of 4.4:1 (needle-1) and 4.3:1 (needle-2).

Based on the measured precipitate composition and the ageing conditions experienced by the sample, the precipitates are identified as α_2 phase. The precipitate volume fractions in needle 1 and 2 were 0.10% and 0.08%, respectively. Equivalent precipitate radius was calculated by approximating the precipitates as spheres. This returns representative precipitate diameters of 1.9 nm for needle 1 and 1.8 nm for needle 2.

4. Discussion

The motivation for this work originated from the initial observation of the core-shell structure observed in primary α grains of a near-α Ti-alloy with bimodal microstructure when using BSE-SEM imaging. It is worth pointing out that such a core-shell structure is also observed by optical microscopy when analysing a sample etched with Kroll's reagent. However, in the latter case, one might assume the darker shell is a result of over-etching.

To exclude the possibility of variations in crystallographic orientation being the root cause for the brighter shell structure in the BSE-SEM images, crystallographic orientation mapping was used to demonstrate that the shell region has the same crystallographic orientation as the core region within a range of approximately 0.3°. In some cases, slightly higher misorientations can be found within primary α grains, which then also results in a change of contrast, but they are not associated with the core-shell structure.

Detailed quantitative chemical mapping using EPMA-WDS, Fig. 4, also revealed a decrease of aluminium (α-stabiliser) and an increase of Mo, Nb, Si, Sn and Zr within the shell area towards the grain/interface boundary. It should be pointed out that this analysis was carried out at relatively low accelerating voltage (7 keV) and therefore the spatial resolution in width and depth was 300 nm, which means that only the

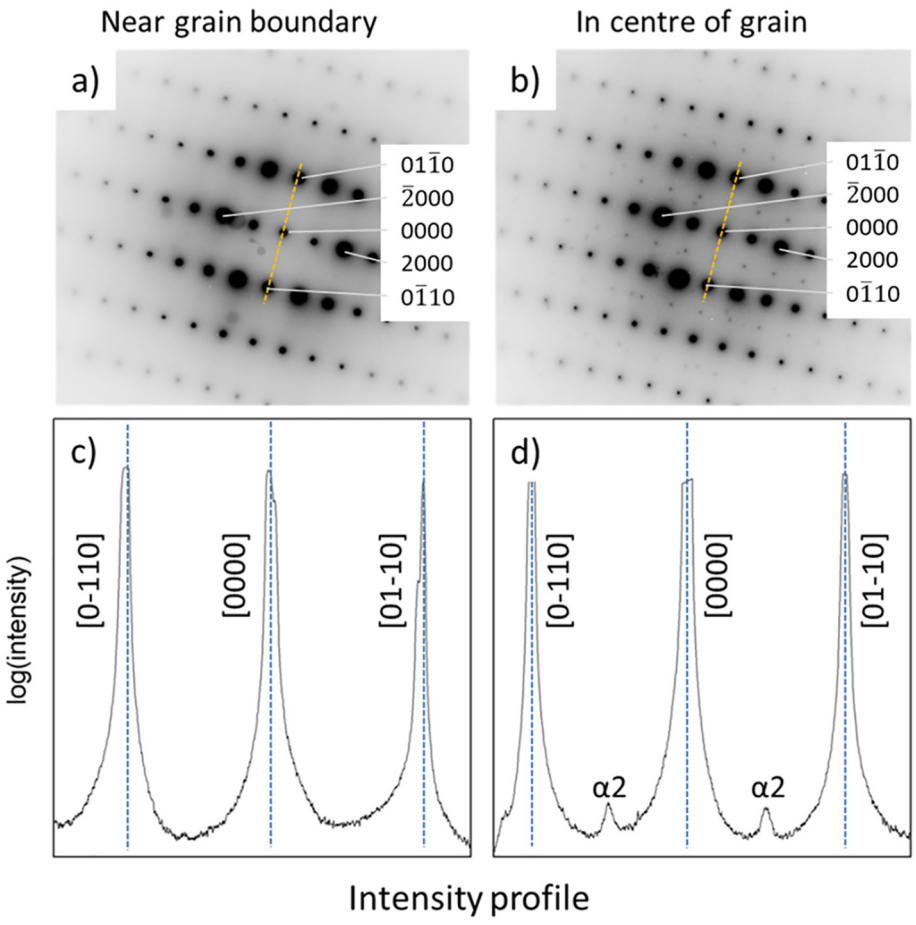

Fig. 6. a), b) Diffraction pattern along [11–20]-zone axis using selective area aperture. **c), d)** Intensity profile for orange lines. Diffraction patterns have been recorded **a), c)** near the grain boundary and **b), d)** the centre of the grain.

data point closest to the α/β phase boundary might be affected by the electron-interaction volume cutting across two phases. Atom probe analysis confirmed both the absolute numbers and relative trends recorded by EPMA-WDS. Considering the variation of the alloying elements within the shell area, i.e. loss of elements lighter than Ti (except Si) and gain of elements heavier than Ti, it becomes clear why the shell appears brighter in BSE-SEM imaging than the core area. It also demonstrates that the shell structure must form during cooling from the sub-β-transus solution temperature, as the β phase at that stage will be depleted in α-stabilisers and enriched in β-stabilisers. It is however interesting to see that Sn and Zr segregate to the β phase, which is apparent from the line scan in Fig. 4, but also from the qualitative

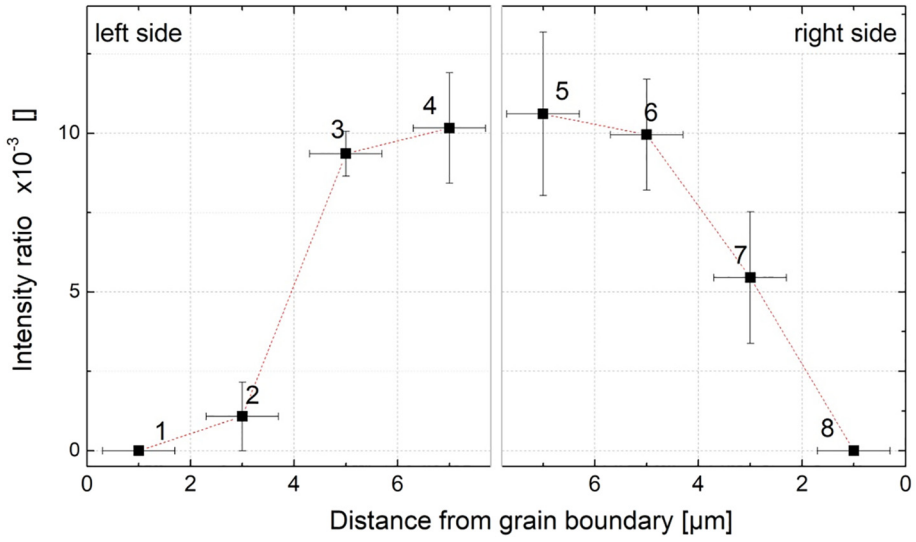

Fig. 7. Ratio of integrated intensity of supperlattice diffraction spot to [0000]-diffraction spot. The number next to the data points identify the areas defined in Fig. 5. The bars in the x-direction indicate the width of areas analysed by selective-area diffraction.

Table 1
Summary of concentrations in wt% for different location determined by EPMA-WDS (see Fig. 4) and APT. Needle-1 and needle-2 are from the centre of the grain, while needle-3 is from close to the grain boundary.

Elements	Concentration wt%					
	EPMA-WDS			APT		
	Centre	Near - GB	Transformed-β	Needle-1	Needle-2	Neddle-3
AL	6.00	5.10	5.30	5.88	6.10	5.42
Sn	3.99	4.41	4.36	3.61	3.69	3.84
Zr	3.01	3.51	3.54	2.94	3.00	3.27
Si	0.38	0.49	0.47	0.37	0.34	0.42
Nb	0.45	0.67	0.72	0.34	0.36	0.46
Mo	0.08	0.34	0.48	0.15	0.12	0.19

Table 2
Chemical composition of α2-precipitates in needle-1 and needle-2.

Element	Concentration (at. %)	
	Precipitates in	
	Needle-1	Needle-2
Ti	79.47	79.07
Al	15.68	16.05
Sn	1.68	1.80
Zr	1.56	1.62
Si	0.64	0.59
Nb	0.17	0.19
Mo	0.07	0.03

chemical maps presented in Fig. 3. The binary phase diagrams of Ti-Sn [30] and Ti-Zr [31] show that for the concentrations of each of the elements in TIMETAL®834, both Zr and Sn are reducing the β-transus temperature. Therefore, Sn and Zr are β-stabilising elements within the given range, which explains the higher concentrations in the transformed β-phase.

The schematic in Fig. 9 is used for explaining the mechanism that leads to the formation of the observed core-shell structure. It is assumed that at the end of the solution heat treatment equilibrium is reached and therefore the chemical composition is constant throughout each of the two phases (Fig. 9a & c). During cooling from the solution temperature, primary α grains grow into the β-phase, which contains relatively low concentrations of α-stabilising elements and high concentrations of β-stabilising elements. Therefore, a shell is formed around primary-α grains, which is depleted in α-stabilising elements, respectively Al, and slightly enriched in β-stabilising elements. Eventually, the β to α phase transformation switches over from growth of primary α to epitaxial growth of secondary α. Throughout the transformation, the β stabilising elements try to escape the approaching β/α interface resulting in the retention of some β-phase at room temperature with increased levels of β stabilisers. However, some of the β-stabilising elements will be trapped in the α-phase as they cannot diffuse away quickly enough. This applies particularly for Mo, due to its low diffusion rate in Titanium [32,33]. One might expect that the trapping of β-stabilisers in the α-phase might increase as cooling proceeds, due to lower diffusion rates at lower temperature. At the same time, it needs to be kept in mind that the equilibrium chemical composition also changes as a function of temperature, which potentially influences local compositions. The growth of secondary α-phase is often initiating at the grain boundaries of primary α grains (Fig. 9**a & b** (r_1 and blue line)) and direction of growth is in radial direction away from the primary α grains (Fig. 9**b**: purple arrow). Therefore, secondary α phase further away from primary α grains has formed at lower temperatures and therefore can be expected to have slightly higher concentrations of β-stabilising elements.

Regarding the low concentrations of Al, Sn and Si in what is suggested to be α_2, characterised by APT, there are two possible explanations for low concentrations. Firstly, the ageing time experienced by the sample was short, meaning the precipitates are in the early stages of α_2 formation and have not had sufficient time to become fully enriched in Al, Sn and Si. Secondly, there is an interface region between matrix and precipitates, as has been shown by Radecka et al. [7]. As the isoconcentration surface of 12 at.% is lower than the Al concentration expected in the α_2 precipitates, it can be assumed that the interface region has been included in our analysis, resulting in a lower average concentration of Al, Sn and Si than expected for Ti_3(Al, Sn, Si).

It is not clear at this stage to what extent the solid solution strengthening effect changes from the core to the shell structure. While less aluminium would reduce solid solution strengthening, the increase of the other elements would increase it again. An important question that arises from the change of aluminium content is if α_2 formation is

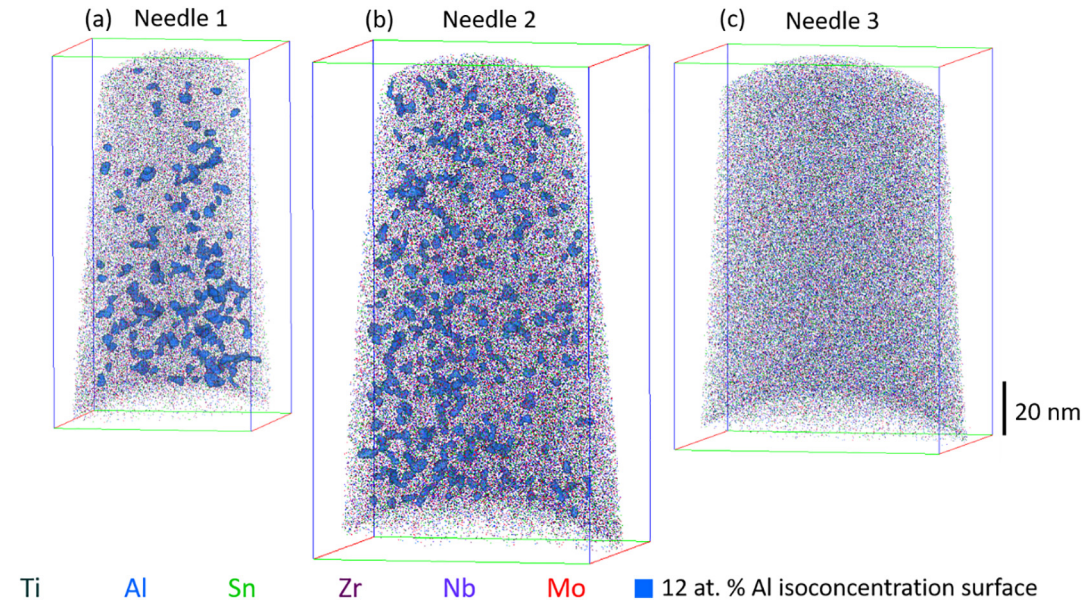

Fig. 8. Atom maps for the needle taken from the centre of the primary-α grain (a), (b) and the needle taken nearest to the grain boundary (c). 12 at.% Al iso surfaces have been used to highlight the precipitates in (a) and (b).

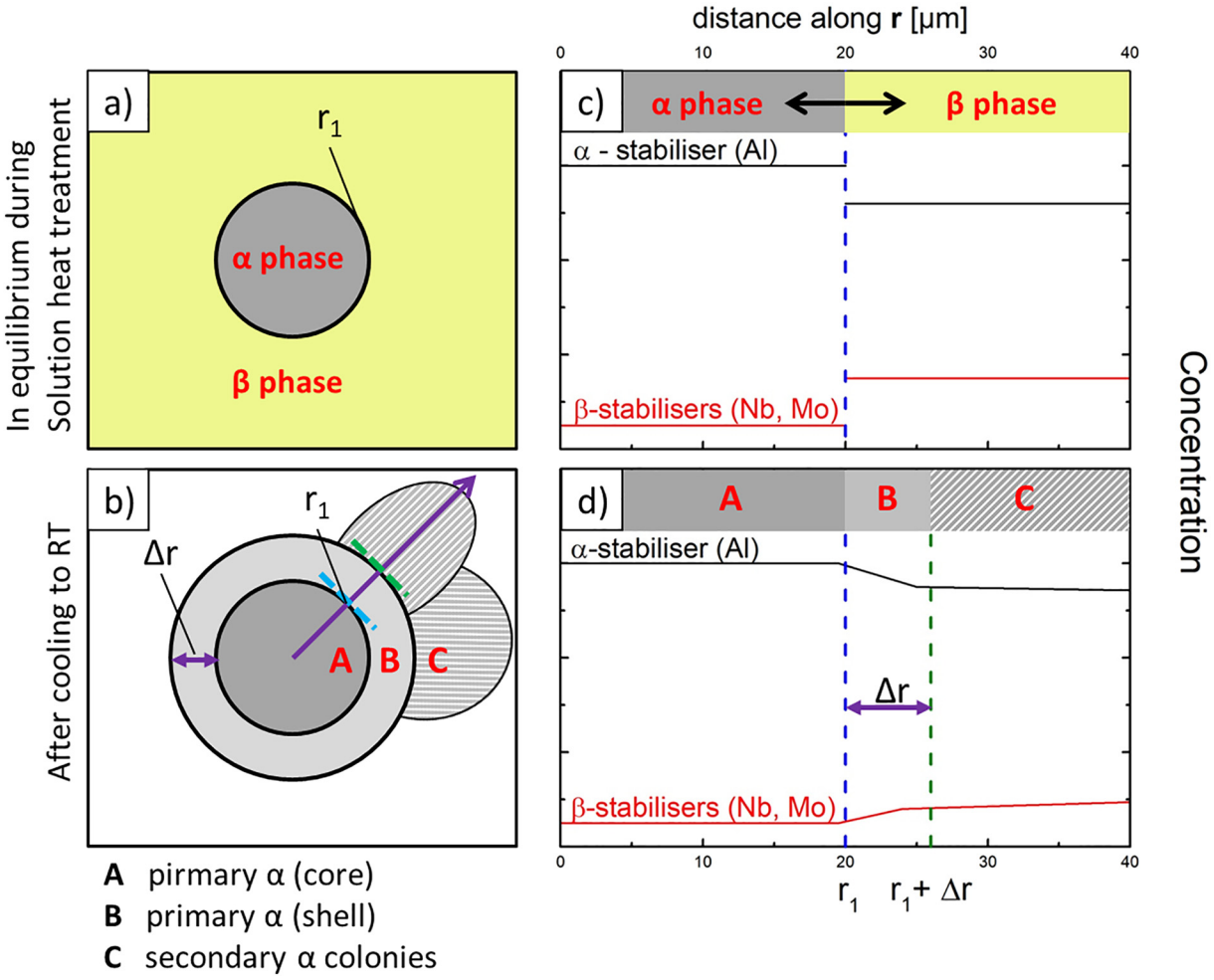

Fig. 9. Schematic drawing of (a & b) and schematic concentration profile across (c & d) a primary α grain during solution heat treatment (a & c) and after cooling to room temperature (b & d). In (c), the concentration profile is plotted for the α grain, as well as the surrounding β phase; in (d) the profile is plotted for the α phase only and the retained β phase in area C is disregarded.

suppressed in the shell area. As pointed out more recently by Radecka et al. [7,8], it is not only aluminium that promotes α_2 formation but also zirconium, silicon, molybdenum and vanadium. Indeed, their work highlighted that tin and silicon are stronger α_2 formers than aluminium. Hence, the observed absence of α_2 precipitates in the shell area studied by SAED in a TEM, as well as in APT, was not a foregone conclusion. The formation of α_2 precipitates is important for a number of reasons. It provides precipitation strengthening, but it also enhances strain localisation [34,35] resulting in greater stress concentrations near grain boundaries and potentially earlier failure. To what extent the absence of α_2 in the shell structure of primary α grains might mitigate against such stress concentration by localised shear is not clear at this stage, but it highlights the potential importance of the present finding.

5. Conclusions

Primary α grain growth during cooling after sub-β-solvus solution heat treatment of a near-α Ti alloy results in chemical segregation, which can be seen in BSE-SEM images in form of a core-shell structure in primary α. Microchemical analysis has shown that the shell has similar chemical composition as secondary α; depleted in Al and enriched in β-stabilising alloying elements. Despite being described as neutral alloying elements in literature, it has been shown that Sn and Zr act as β-stabilising elements. The reduced concentration of Al near the grain/interface boundary results in the absence of α_2 despite high level of Sn and Si that also promote α_2 formation, while α_2 has been found in the centre of primary α grains.

Acknowledgement

The authors would like to thank the EPSRC funding the project through the CDT in Advanced Metallic Systems. The authors would also like to thank Rolls-Royce plc and TIMET for providing additional funding and the provision of material.

This work was supported by the Henry Royce Institute for Advanced Materials, funded through EPSRC grants EP/R00661X/1, EP/S019367/1, EP/P025021/1 and EP/P025498/1.

We are grateful for the use of the JEOL JXA-8530F FEG-EPMA, EPSRC award EP/M028097/1. We would like to thank Jonathan Fellowes for his support with EPMA-WDS experiment and data analysis.

We would like to acknowledge Matthew Topping and Xu Xu for their help with TEM experiment and sample preparation.

Data availability statement

The datasets generated during and/or analysed during the current study are available from the corresponding author on reasonable request.

Declaration of competing interest

The authors declare that they have no known competing financial

interests or personal relationships that could have appeared to influence the work reported in this paper.

Appendix A. Supplementary data

Supplementary data to this article can be found online at https://doi.org/10.1016/j.matchar.2020.110327.

References

[1] G. Lütjering, J.C. Williams, Titanium: Engineering Materials and Processes, second edi, Springer, 2007, pp. 1–442, https://doi.org/10.1007/978-3-540-73036-1.

[2] H. Conrad, Effect of interstitial solutes on the strength and ductility of titanium, Prog. Mater. Sci. 26 (1981) 123–403, https://doi.org/10.1016/0079-6425(81)90001-3.

[3] H.W. Rosenberg, W.D. Nix, Solid solution strengthening in Ti-Al alloys, Metall. Trans. 4 (1973) 1333–1338.

[4] E.W. Collings, H.L. Gegel, A physical basis for solid-solution strengthening and phase stability in alloys of titanium, Scr. Metall. 7 (1973) 437–443, https://doi.org/10.1016/0036-9748(73)90092-6.

[5] G. Lütjering, S. Weissmann, Mechanical properties of age-hardened titanium-aluminum alloys, Acta Metall. 18 (1970) 785–795, https://doi.org/10.1016/0001-6160(70)90043-X.

[6] T.K.G. Namboodhiri, C.J. McMahon, H. Herman, Decomposition of the α-phase in titanium-rich Ti-Al alloys, Metall. Trans. 4 (1973) 1323–1331.

[7] A. Radecka, J. Coakley, V.A. Vorontsov, T.L. Martin, P.A.J. Bagot, M.P. Moody, D. Rugg, D. Dye, Precipitation of the ordered α2 phase in a near-α titanium alloy, Scr. Mater. 117 (2016) 81–85, https://doi.org/10.1016/j.scriptamat.2016.02.015.

[8] A. Radecka, P.A.J. Bagot, T.L. Martin, J. Coakley, V.A. Vorontsov, M.P. Moody, H. Ishii, D. Rugg, D. Dye, The formation of ordered clusters in Ti-7Al and Ti-6Al-4V, Acta Mater. 112 (2016) 141–149, https://doi.org/10.1016/j.actamat.2016.03.080.

[9] O.N. Senkov, J.J. Valencia, S.V. Senkova, M. Cavusoglu, F.H. Froes, Effect of cooling rate on microstructure of Ti-6Al-4V forging, Mater. Sci. Technol. 18 (2002) 1471–1478, https://doi.org/10.1179/026708302225007808.

[10] B.S.S.C. Rao, M. Srinivas, S.V. Kamat, The effect of volume fraction of primary α phase on fracture toughness behaviour of Timetal 834 titanium alloy under mode I and mixed mode I/III loading, Mater. Sci. Eng. A 520 (2009) 29–35, https://doi.org/10.1016/j.msea.2009.05.007.

[11] K.V.S. a I. Srinadh, N. Singh, V. Singh, Role of Ti3Al/silicides on tensile properties of Timetal 834 at various temperatures, Bull. Mater. Sci. 30 (2007) 595–600.

[12] A. Kumar, N. Singh, V. Singh, Influence of stabilization treatment on low cycle fatigue behavior of Ti alloy IMI 834, Mater. Charact. 51 (2003) 225–233, https://doi.org/10.1016/j.matchar.2003.11.004.

[13] A.K. Singh, C. Ramachandra, Characterization of silicides in high-temperature titanium alloys, J. Mater. Sci. 32 (1997) 229–234, https://doi.org/10.1023/A:1018516324856.

[14] G.B. Thompson, M.K. Miller, H.L. Fraser, Some aspects of atom probe specimen preparation and analysis of thin film materials, Ultramicroscopy 100 (2004) 25–34, https://doi.org/10.1016/j.ultramic.2004.01.010.

[15] K. Thompson, D. Lawrence, D.J. Larson, J.D. Olson, T.F. Kelly, B. Gorman, In situ site-specific specimen preparation for atom probe tomography, Ultramicroscopy 107 (2007) 131–139, https://doi.org/10.1016/j.ultramic.2006.06.008.

[16] G.E. Lloyd, Atomic number and crystallographic contrast images with the SEM: a review of backscattered Electron techniques, Mineral. Mag. 51 (1987) 3–19, https://doi.org/10.1180/minmag.1987.051.359.02.

[17] W. Reuter, Electron Probe Microanalysis, 25 (1971), pp. 80–119.

[18] D. Drouin, A.R. Couture, R. Gauvin, monte CArlo, Simulation of electroN Trajectory in sOlids Casino, (2011).

[19] A.P. Woodfield, P.J. Postans, M.H. Loretto, R.E. Smallman, The effect of long-term high temperature exposure on the structure and properties of the titanium alloy Ti 5331S, Acta Metall. 36 (1988) 507–515, https://doi.org/10.1016/0001-6160(88)90082-X.

[20] N. Mori, T. Oikawa, T. Katoh, J. Miyahara, Y. Harada, Application of the “imaging plate” to TEM image recording, Ultramicroscopy 25 (1988) 195–201, https://doi.org/10.1016/0304-3991(88)90014-9.

[21] B.H. Armstrong, Spectrum line profiles: the Voigt function, J. Quant. Spectrosc. Radiat. Transf. 7 (1967) 61–88, https://doi.org/10.1016/0022-4073(67)90057-X.

[22] D.J. Larson, T. Prosa, R.M. Ulfig, B.P. Geiser, T.F. Kelly, Local Electrode Atom Probe Tomography, US Springer Sci, New York, 2013.

[23] M.P. Moody, L.T. Stephenson, A.V. Ceguerra, S.P. Ringer, Quantitative binomial distribution analyses of nanoscale like-solute atom clustering and segregation in atom probe tomography data, Microsc. Res. Tech. 71 (2008) 542–550, https://doi.org/10.1002/jemt.20582.

[24] T. Homma, A. Arafah, D. Haley, M. Nakai, M. Niinomi, M.P. Moody, Effect of alloying elements on microstructural evolution in oxygen content controlled Ti-29Nb-13Ta-4.6Zr (wt%) alloys for biomedical applications during aging, Mater. Sci. Eng. A 709 (2018) 312–321, https://doi.org/10.1016/J.MSEA.2017.10.018.

[25] C.A. Williams, D. Haley, E.A. Marquis, G.D.W. Smith, M.P. Moody, Defining clusters in APT reconstructions of ODS steels, Ultramicroscopy 132 (2013) 271–278, https://doi.org/10.1016/j.ultramic.2012.12.011.

[26] A.J. London, Quantifying uncertainty from mass-peak overlaps in atom probe microscopy, Microsc. Microanal. 25 (2019) 378–388, https://doi.org/10.1017/S1431927618016276.

[27] F. De Geuser, B. Gault, Metrology of Small Particles and Solute Clusters by Atom Probe Tomography, http://arxiv.org/abs/1910.10532, (2019).

[28] B. Gault, M.P. Moody, J.M. Cairney, S.P. Ringer, Atom probe microscopy, Springer Science & Business Media, 2012.

[29] C.Y. Jones, W.E. Luecke, E. Copland, Neutron diffraction study of oxygen dissolution in α2- Ti3Al, Intermetallics 14 (2006) 54–60, https://doi.org/10.1016/j.intermet.2005.04.011.

[30] F. Yin, J.-C. Tedenac, F. Gascoin, Thermodynamic modelling of the Ti–Sn system and calculation of the co–Ti–Sn system, Calphad 31 (2007) 370–379, https://doi.org/10.1016/J.CALPHAD.2007.01.003.

[31] K.C. Hari Kumar, P. Wollants, L. Delacy, Thermodynamic assessment of the Ti-Zr system and calculation of the Nb-Ti-Zr phase diagram, J. Alloys Compd. 206 (1994) 121–127, https://doi.org/10.1016/0925-8388(94)90019-1.

[32] R.P. Elliott, Diffusion in titanium and titanium alloys, Armour Research Foundation, Chicago IL, https://apps.dtic.mil/dtic/tr/fulltext/u2/290336.pdf, (1962).

[33] G.B. Gibbs, D. Graham, D.H. Tomlin, Diffusion in titanium and titanium—niobium alloys, Philos. Mag. 8 (1963) 1269–1282.

[34] D. Lunt, X. Xu, T. Busolo, J. Quinta da Fonseca, M. Preuss, Quantification of strain localisation in a bimodal two-phase titanium alloy, Scr. Mater. 145 (2018) 45–49, https://doi.org/10.1016/j.scriptamat.2017.10.012.

[35] D. Lunt, T. Busolo, X. Xu, J. Quinta da Fonseca, M. Preuss, Effect of nanoscale α2 precipitation on strain localisation in a two-phase Ti-alloy, Acta Mater. 129 (2017) 72–82, https://doi.org/10.1016/J.ACTAMAT.2017.02.068.